



Article

Diatom Biosilica Doped with Palladium(II) Chloride Nanoparticles as New Efficient Photocatalysts for Methyl Orange Degradation

Myroslav Sprynskyy ^{1,2,*} , Paulina Szczyglewska ³, Izabela Wojtczak ^{1,2}, Izabela Nowak ³ , Andrzej Witkowski ⁴ , Bogusław Buszewski ^{1,5} and Agnieszka Feliczak-Guzik ^{3,*}

¹ Faculty of Chemistry, Nicolaus Copernicus University in Toruń, 7 Gagarina Str., 87-100 Toruń, Poland; izabelawojtczak1991@gmail.com (I.W.); bbusz@chem.umk.pl (B.B.)

² Department of Biopharmaceutics and Pharmacodynamics, Medical University of Gdańsk, Hallera 107, 80-416 Gdańsk, Poland

³ Faculty of Chemistry, Adam Mickiewicz University in Poznań, Uniwersytetu Poznańskiego 8, 61-614 Poznań, Poland; paulina.debek@amu.edu.pl (P.S.); nowakiza@amu.edu.pl (I.N.)

⁴ Institute of Marine and Environmental Sciences, University of Szczecin, Mickiewicza 16A, 70-383 Szczecin, Poland; andrzej.witkowski@usz.edu.pl

⁵ Centre for Modern Interdisciplinary Technologies, Nicolaus Copernicus University in Toruń, Wileńska 4, 87-100 Toruń, Poland

* Correspondence: mspryn@chem.umk.pl (M.S.); agaguzik@amu.edu.pl (A.F.-G.); Tel.: +48-618-291-747 (A.F.-G.)



Citation: Sprynskyy, M.; Szczyglewska, P.; Wojtczak, I.; Nowak, I.; Witkowski, A.; Buszewski, B.; Feliczak-Guzik, A. Diatom Biosilica Doped with Palladium(II) Chloride Nanoparticles as New Efficient Photocatalysts for Methyl Orange Degradation. *Int. J. Mol. Sci.* **2021**, *22*, 6734. <https://doi.org/10.3390/ijms22136734>

Academic Editor: Luisa Margarida Martins

Received: 31 May 2021
Accepted: 20 June 2021
Published: 23 June 2021

Publisher's Note: MDPI stays neutral with regard to jurisdictional claims in published maps and institutional affiliations.



Copyright: © 2021 by the authors. Licensee MDPI, Basel, Switzerland. This article is an open access article distributed under the terms and conditions of the Creative Commons Attribution (CC BY) license (<https://creativecommons.org/licenses/by/4.0/>).

Abstract: A new catalyst based on biosilica doped with palladium(II) chloride nanoparticles was prepared and tested for efficient degradation of methyl orange (MO) in water solution under UV light excitation. The obtained photocatalyst was characterized by X-ray diffraction, TEM and N₂ adsorption/desorption isotherms. The photocatalytic degradation process was studied as a function of pH of the solution, temperature, UV irradiation time, and MO initial concentration. The possibilities of recycling and durability of the prepared photocatalysts were also tested. Products of photocatalytic degradation were identified by liquid chromatography–mass spectrometry analyses. The photocatalyst exhibited excellent photodegradation activity toward MO degradation under UV light irradiation. Rapid photocatalytic degradation was found to take place within one minute with an efficiency of 85% reaching over 98% after 75 min. The proposed mechanism of photodegradation is based on the assumption that both HO• and O₂•[−] radicals, as strongly oxidizing species that can participate in the dye degradation reaction, are generated by the attacks of photons emitted from diatom biosilica (photonic scattering effect) under the influence of UV light excitation. The degradation efficiency significantly increases as the intensity of photons emitted from biosilica is enhanced by palladium(II) chloride nanoparticles immobilized on biosilica (synergetic photonic scattering effect).

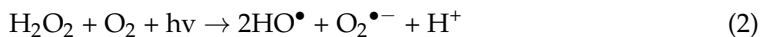
Keywords: diatom biosilica; palladium(II) nanoparticles; photocatalysis; methyl orange photodegradation

1. Introduction

Every year, more than 0.7 million tons of dyestuffs and synthetic pigments are produced globally, among approximately 10,000 dyestuffs used on an industrial scale [1,2]. More than half of them are azo dyes (e.g., methyl orange), which are used by the textile and dye industry [3,4]. Therefore, in recent decades, elimination of azo dyes from wastewater has been a serious problem, as they contribute both to environmental pollution and to eutrophication, which affects the functioning of aquatic organisms [5–7]. The current methods used for wastewater treatment are mainly based on physicochemical techniques. These include chemical precipitation and subsequent separation of pollutants, electrocoagulation and adsorption. These techniques, however, do not ensure complete removal of the pollutants and may generate additional, secondary environmental pollution [8–10].

One of the most effective methods of removing organic compounds, including dyes, is the use of highly efficient and multi-stage technologies, which include advanced oxidation

processes (AOPs) [11–14]. The mechanism of these processes is based on the use of high potentials of hydroxyl radicals HO•, which can be generated in various ways, e.g., [15]:



One example of AOPs is photocatalysis. In this process, hydroxyl radicals are generated under the influence of UV radiation, the oxidizing effect of these radicals leads to degradation of many organic pollutants present in the environment. Photocatalytic recuperation takes place by converting photon energy into chemical energy [15–17].

In recent years, the degradation of toxic organic pollutants using heterogeneous photocatalysts has been intensively studied [18–22]. TiO₂ has been considered one of the best photocatalysts [23]. However, its range of light response and photoelectric efficiency is limited due to the width of the energy gap—3.2 eV [23]. Apart from TiO₂, other photocatalysts have been used in the process of degradation of organic pollutants and water splitting under the influence of visible light irradiation, including: BiVO₄ [24], CdS [25], Bi₂WO₆ [26], gamma-C₃N₄ [27–29], BiFeO₃ [30]. However, low specific surface area and fast rate of recombination of photogenerated charge carriers significantly reduce photocatalytic efficiency of these materials [17]. Therefore, one of the ways to increase the efficiency of a photocatalyst is to immobilize it on different media. Examples of such media are: glass or polymer fibres, silica, steel or glass plates, optical fibres or membranes. The material subjected to immobilization should meet the following criteria: it should be transparent to UV radiation, chemically resistant and easily separable from the solution [31].

The aim of this study was to develop an effective method of azo dye degradation, i.e., methyl orange (MO), based on a photocatalytic process using palladium(II) chloride-doped diatom biosilica and UV irradiation. The specific objectives of the study were: characterization of the kinetics of temperature-dependent photocatalytic degradation of MO, assessment of the efficiency of MO photocatalytic degradation depending on the pH of the solution and on the initial concentration of MO in the solution, identification of the products of photocatalytic degradation of MO, checking the possibility of recycling and evaluation of the durability of the prepared photocatalyst.

Diatoms are unicellular photosynthetic algae having shells (exoskeletons, frustules, carapaces) composed of amorphous, hydrated silica. These frustules consist of two overlapping shells called thecae (upper part—epitheca, lower—hypotheca) with a characteristic bilateral Petri dish-like structure [32–36].

The siliceous walls of diatom frustules are decorated by original pattern of ordered structural features such as pores, ridges, ribs, spikes or spines creating the most spectacular example of three-dimensional (3D) structured silica materials of biological origin. The diatom's frustule surface contains a high level of the silanol groups (Si-OH) and siloxane bridges (Si-O-Si) [34,35,37].

The perfectly ordered three-dimensional structure, thermal and mechanical resistance, unique optical properties and biocompatibility make diatom biosilica a valuable raw material for the development of modern technologies, it can be used to produce optoelectronic devices, biosensors, gas sensors, catalysts, light harvesting materials, adsorbents, efficient filters, semiconductors, solar cells, templates for nanolithography, drug carriers or building materials in the synthesis of bone implants [33,36]. In addition, the multitude of applications of diatom biosilica may be due to the possibility of modifying its physicochemical properties to obtain new silica functional materials while maintaining a unique 3D structure [38]. Moreover, silica frustules isolated from cultures of diatoms show high photoluminescence activity associated with the emission in the mid-ultraviolet (290–300 nm) under UV irradiation, emission (493 nm) and excitation (480 nm) in the narrow blue region, and emission in the green region (498–525 nm) of the visible spectrum under UV irradiation [39].

In turn, catalysts modified with palladium compounds are often used in various organic reactions. The synthesis of palladium nanoparticles of various sizes (from 1 to tens of nanometres) and shapes, is carried out by chemical reduction [40,41] or electrochemical deposition [42] in aqueous solutions.

To the best of our knowledge, there are only a small number of literature reports describing the properties of palladium(II) nanoparticles made from chloride source. These compounds exhibit high thermal and mechanical stability and catalytic activity [43,44].

According to previously published reports, diatomaceous biosilica was functionalized with TiO_2 to use as effective photocatalysts for indoor air purification [45,46], for photocatalytic degradation of rhodamine B [47,48], as catalyst for dye methyl blue photodegradation [49], and as photocatalysts in the abatement of acetaldehyde [50]. TiO_2 -doped diatom frustules has been tested for their activity in the photocatalytic degradation of the Congo red dye in water [51]. The produced diatom-FeOx composite was evaluated as catalyst in photodegradation of Rhodamine-6G [52]. Diatom biosilica modified with bio-inspired polydopamine and silver nanoparticles was used as active catalyst for dye degradation both, the cationic methylene blue and anionic Congo red dyes [53].

2. Results

2.1. Photocatalyst Characterization

Figure 1 shows the X-ray diffraction patterns of diatom biosilica and palladium(II) chloride-doped diatom biosilica. The wide-angle diffractogram of pristine (unmodified material) shows one main reflection at $2\theta = 22.3^\circ$ indicating the amorphous nature of the biosilica. According to Sprynskyy et al. [39], this XRD pattern is characteristic for opal-A (biogenic amorphous silica).

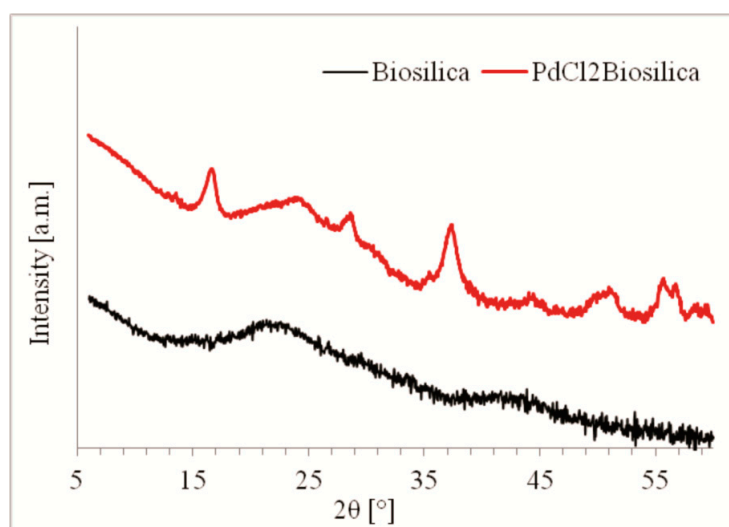


Figure 1. XRD patterns of the samples of pure diatom biosilica and palladium(II) chloride-doped diatom biosilica photocatalyst.

The X-ray diffraction pattern of the palladium(II)-doped diatom biosilica, recorded in a wide-angle range of 2θ permitted identification of palladium(II) chloride nanoparticles on the basis of the reflexes characteristic of this compound at 16.7° , 27.1° , 28.7° , 37.7° , 50.1° , 51.6° , 56.0° , 57.1° (Ref. Code: 00-001-0228).

The low-temperature nitrogen adsorption/desorption isotherms of diatom biosilica and PdCl₂ biosilica are presented in Figure 2. According to the IUPAC classification, the adsorption/desorption isotherm belongs to combination types I and II [54]. Type I is characteristic of microporous materials having relatively small external surfaces, while type II corresponds to nonporous or macroporous materials. The isotherm recorded for

the obtained materials shows a hysteresis loop of H4 type, which indicates the presence of straight slit pores [55].

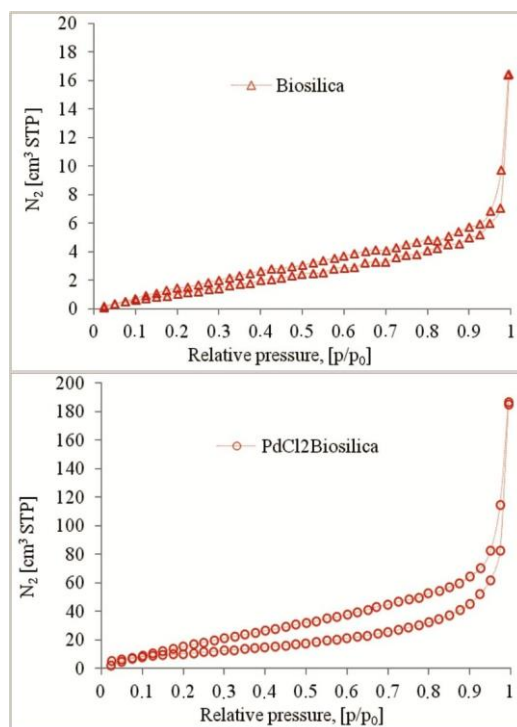


Figure 2. N₂ adsorption isotherms of the pure diatom biosilica and palladium(II) chloride-doped diatom biosilica.

Table 1 shows the values of textural parameters such as the specific surface area, pore volume and average pore diameter obtained on the basis of the isotherm data. The specific surface area of the materials was determined using the BET (Brunauer–Emmett–Teller) method. Pore size distributions were calculated using the KJS (Kruk–Jaroniec–Sayari) method [56] based on the BJH (Barrett–Joyner–Halenda) algorithm.

Table 1. Porous structure parameters of the samples studied.

Sample	Specific Surface Area [m ² g ⁻¹]	Pore Volume [cm ³ g ⁻¹]	Average Pore Diameter [nm]
Biosilica	30	0.43	3.93
PdCl ₂ Biosilica	40	0.28	4.45

The materials obtained have relatively low surface areas (BET), from ~30 m²/g for pure diatom biosilica to ~40 m²/g for palladium(II)-doped diatom biosilica. The average pore diameter varies from 3.93 to 4.45 nm. The total pore volume reaches over 0.28 cm³/g.

The TEM micrographs (Figure 3) revealed the morphology and structure of the tested palladium(II) chloride-doped diatom biosilica photocatalyst and the palladium(II) chloride nanoparticles distribution.

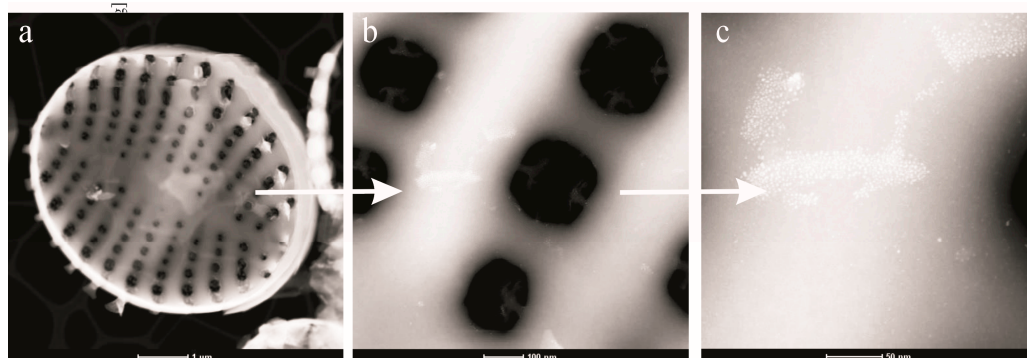


Figure 3. TEM micrographs of the palladium(II) chloride-doped diatom biosilica photocatalyst. Ordered periodic pore system (a), the morphology and structure of periodic pores (b), and the size, forms and specificity of the distribution of immobilized palladium(II) chloride nanoparticles (c).

The TEM images demonstrate the three-dimensional structure of a single diatom valve whose walls are perforated by an ordered periodic pore system (Figure 3a), the morphology and structure of periodic pores (Figure 3b), and the size, forms and specificity of the distribution of immobilized palladium(II) chloride nanoparticles (Figure 3c). The periodic pores are oval in shape, and their size ranges from 150 to 200 nm (arrow in Figure 3b). The arrow in Figure 3c shows that nanoparticles of palladium(II) chloride on the surface of diatom biosilica form single-layer clusters in the form of islets (flakes) of various configurations. These islets have dimensions ranging from about 10 to 100 nanometres along the long axis and contain from several to several hundred nanoparticles. The palladium(II) chloride nanoparticles with irregular shapes with diameters ranging of 2–3 nm adhere tightly to the biosilica surface. The very small size of the nanoparticles and their good dispersion on the biosilica surface can also contribute to the high efficiency of photodegradation.

2.2. Photocatalytic Activity

2.2.1. MO Photocatalytic Degradation Depending on the pH Value

The dependence of MO photocatalytic degradation on pH values and temperature is shown in Figure 4. The photocatalytic activities of the PdCl₂ biosilica and biosilica toward methyl orange was determined under UV light irradiation. Preliminary tests of the adsorption capacities of both the PdCl₂ biosilica and biosilica in the dark showed a negligible effectiveness of a few percent. Similarly, it was found that the MO degradation does not occur in the dark and in the presence of TiO₂ photocatalyst [57]. Initially blank test performed under UV irradiation without catalyst also showed negligible degradation effects.

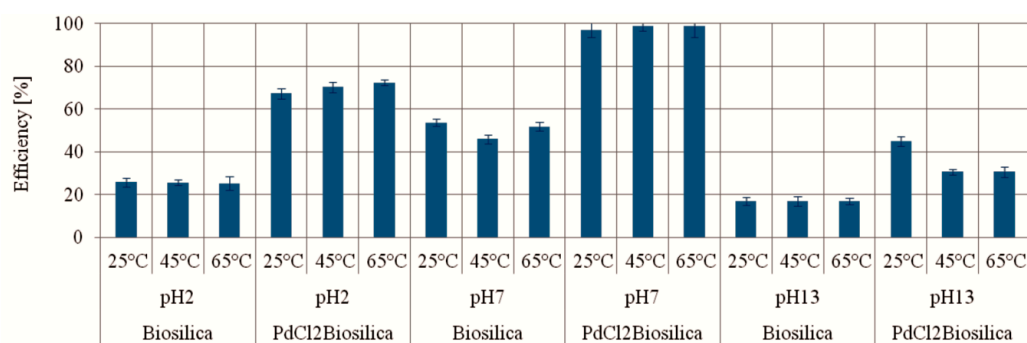


Figure 4. The efficiency of MO photocatalytic degradation for different pH value and temperature. Experimental conditions: $t = 90$ min; m (Biosilica)—10 mg; C_0 (MO)—9.98 mg/L; V (MO solution)—15 mL.

The results show that the biosilica and PdCl₂ biosilica exhibit different abilities to induce photocatalytic degradation of MO in various pH conditions: acid, neutral and

alkaline. The efficiency of MO degradation was almost twice higher for PdCl₂ biosilica compared to unmodified biosilica under all pH conditions. The maximum efficiency of MO degradation (52% for biosilica and 98% for PdCl₂Biosilica) was achieved in a neutral medium at pH 7. A fairly high efficiency (72%) of MO degradation in an acid medium was obtained in the presence of PdCl₂Biosilica. The temperature increase in the range from 25 to 65 °C did not show a visible impact on the effectiveness of the photocatalytic degradation of the dye (see Figure 5).

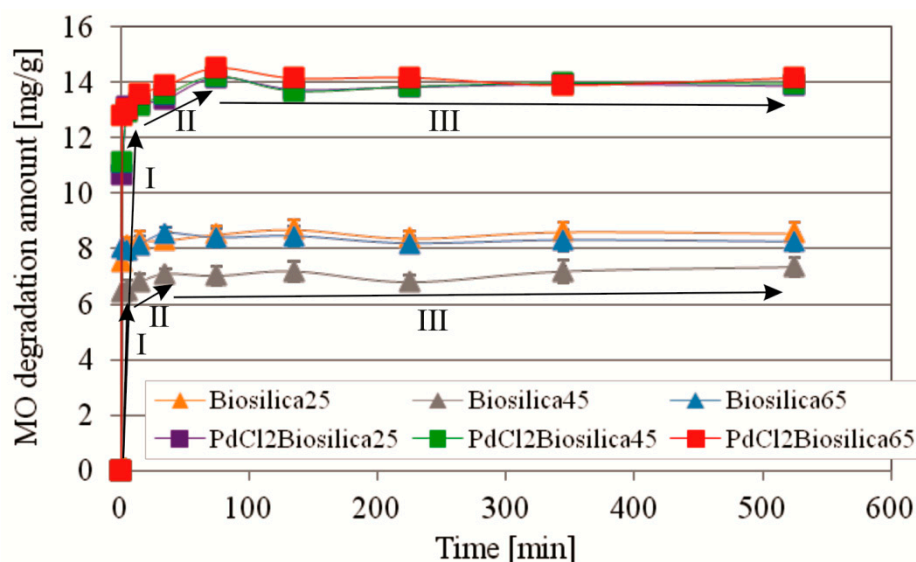


Figure 5. Kinetic curves of MO photocatalytic degradation under UV irradiation using PdCl₂ biosilica and biosilica photocatalyst. Experimental conditions: m (Biosilica)—10 mg; T = 25 °C; C₀(MO)—9.98 mg/L; V (MO solution)—15 mL; pH—7.0.

Literature reports on methyl orange degradation in aqueous solutions using different types of photocatalysts give different pH values at which the maximum efficiency of the dye decomposition is achieved. The highest efficiency of dye degradation/sorption was obtained in an acidic medium at pH 3 using such photocatalysts as TiO₂ [57,58], MnO₂-decorated diatomite [59], polymeric chitosan-isovanillin [60], and at pH 2 using TiO₂, Au/TiO₂ composites [61] or Black Sand [62]. The optimum pH value for MO removal from aqueous solution using chitosan/diatomite composite was 5 [63]. Photodegradation of MO by chitosan embedded with nano-CdS was the most efficient (99%) at pH 4, but a high level of degradation (80%) was also observed at pH 6 and pH 8 [64]. The high degradation efficiency of MO in both strong acidic and near neutral environments was observed for Fe-based metallic glass [65]. Experimental results of MO photocatalytic degradation in the presence of TiO₂/ASS also showed that the process rate was the highest at pH 7 [66]. The maximum efficiency of MO photodegradation was obtained for pH from the basic range, pH8 in the presence of TiO₂ catalyst and at pH9 [67] in the presence of MnWO₄ under UV radiation [68]. The increase in the conversion of MO with pH increasing from 6 to 11 was observed for MO photocatalytic degradation over TiO₂ nanotubes [69]. The proposed explanation of this phenomenon is that the hydroxyl radicals formed in alkaline medium in the reaction ($\text{OH}^- + \text{h}^+ = \text{OH}^\bullet$) can be more reactive toward the dye at higher pH [69]. However, according to the results obtained by Tokode and co-workers [70], the photonic efficiency of the MO degradation in the aqueous phase at the presence of TiO₂ catalysts is comparable with that achieved in our study, irrespective of pH. This indicates that MO may be decomposed by both oxidative and reductive mechanisms in the photocatalytic process [70].

We hypothesise that both HO[•] and O₂^{•-} radicals as highly oxidizing species can be generated from diatom biosilica by attacks of emitted photons under UV light excitation and both of them can be involved in the reaction mechanism of MO degradation. The

energy of the emitted photons can be absorbed by water molecules on the biosilica surface leading to generation of HO^\bullet and $\text{O}_2^{\bullet-}$ radicals. The emitted photons may also directly interact with the dye molecule, causing its degradation. In the process of MO degradation in the presence of diatom biosilica doped with PdCl_2 nanoparticles, the photocatalytic effect was over twice as high as that in the presence of pure diatom biosilica (Figure 4). As reported in [71], the photocatalytic activity of $\text{Bi}_2\text{WO}_6/\text{SiO}_2$ photonic crystal film was observed to be about three times higher than that of the ordinary Bi_2WO_6 film in the photocatalytic decomposition of Rhodamine B (RhB) and phenol. These results confirmed a significant role of photonic crystals in photocatalytic processes. The photosensitive photonic crystals are promising for design and production of the synergistic photonic crystals based on plasmonic photocatalysts of plasmonic and photonic nanostructures [72].

2.2.2. Kinetics of MO Photocatalytic Degradation at Different Temperatures

The kinetics of MO photocatalytic degradation at different temperatures under UV irradiation using PdCl_2 biosilica and biosilica are shown in Figure 5. The kinetics is expressed by kinetic curves revealing three different stages of MO photocatalytic degradation. The initial rapid stage is followed by the second much slower process, and then by the stage of equilibrium with the weak fluctuation effects. The character of the process is very similar for biosilica and PdCl_2 biosilica (the shape of the kinetic curves is the same), but the dye degradation efficiency is almost twice as high for PdCl_2 biosilica as for Biosilica. In the initial step, rapid photocatalytic degradation of the test dye takes place within one minute with an efficiency of about 45% and 85% for biosilica and PdCl_2 biosilica, respectively. The second stage lasts for about 35 min with the use of biosilica and about 75 min using PdCl_2 biosilica. After reaching equilibrium, the maximum efficiency for the two tested biosilica samples was 56% and 97%, for pristine and modified samples respectively. The high efficiency of MO photocatalytic degradation in the very rapid first stage may indicate that the surface layer reactions control the process. The contact time required to achieve equilibrium (75 min) was used in the next batch study of the isotherm of MO photocatalytic degradation over PdCl_2 biosilica at 25 °C.

Similarly, high efficiency (95–99%) of MO photocatalytic degradation was achieved using Pt modified with TiO_2 [73], Ag/HSTiO₂ [74], chitosan with immobilized nano-CdS [64], TiO_2 -CuZSM-5 [75], scoria-Ni/ TiO_2 [76], and TiO_2 /ZnO mixture [77] after 90, 90, 80, 70, 45, 30 min UV radiation time, respectively. Significantly more time (240 min) was required to reach the maximum efficiency (90%) of MO degradation in the presence of graphene oxide supported titanium dioxide (GO/ TiO_2) composites [78]. A photocatalytic degradation rate of 87% in the same time of 240 min was observed for Cu-doped ZnO nanoparticles [79], while the highest photocatalytic efficiency (50%) of MnWO_4 was obtained only after 480 min [68].

For comparison, the photocatalytic degradation of MO using only a palladium(II) chloride and commercial amorphous silica doped with PdCl_2 (PdCl_2 _SiO₂) as catalysts was also studied (Figure 6). The shape of the MO degradation kinetic curves using pure PdCl_2 and biosilica doped with PdCl_2 differs significantly. In the case of PdCl_2 a much slower dye degradation process and a correspondingly much delayed time (345 min) to reach equilibrium were observed. Once equilibrium was reached, the maximum MO degradation efficiency over PdCl_2 was 87%. Photocatalytic degradation of the dye by commercial amorphous silica also occurs much slower compared to pure biosilica or PdCl_2 biosilica and the maximum efficiency of MO degradation during equilibrium is only 32%.

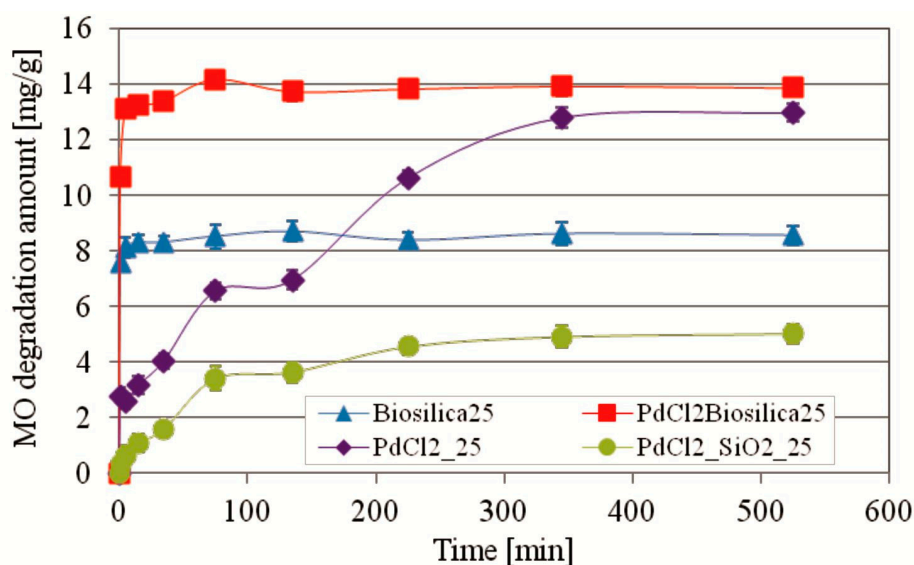


Figure 6. The comparison of the kinetics curves of MO photocatalytic degradation using PdCl₂ biosilica and biosilica photocatalysts with the kinetics curves of MO photocatalytic degradation by pure PdCl₂ and commercial amorphous silica doped with PdCl₂. Experimental conditions: m (biosilica)—10 mg; T = 25 °C; C₀(MO)—10.25 mg/L; V (MO solution)—15 mL; pH—7.0.

To explain the possible mechanisms of MO photocatalytic degradation in the presence of diatom biosilica doped with palladium(II) chloride nanoparticles, the experimental kinetics data were approximated with the pseudo-zero-order, Lagergren pseudo-first-order, pseudo-second-order, and Weber–Morris intraparticle diffusion models. According to determination coefficient values (R^2) of the models fitting, the MO photocatalytic degradation was significantly better described by the pseudo-second-order kinetic model than by the pseudo-first-order kinetic model. This means that the degradation rate of the process is heterogenic and depends on several factors. The results of the study of photocatalytic degradation of MO in the presence of chitosan with immobilized nano-CdS [64], TiO₂ nanoparticles [80], and polymeric chitosan-isovanillin [60] indicated that the kinetics of the photocatalytic degradation over these catalysts followed the pseudo-first-order kinetic model. The pseudo-zero-order kinetic model describes the first and second stages of the kinetic curves as linear functions and permits direct determination of values mg/g/min of photocatalytic degradation rate. The photocatalytic degradation rate in the first stage is almost hundred times higher than that in the second stage. According to the obtained results of Weber–Morris model fitting, two mechanisms are involved in the kinetic processes of photocatalytic degradation. The value of constant A indicates that the majority of MO is retained in the boundary layer and suggest that the photocatalytic degradation rate is mainly governed by the external surface reactions. This mechanism dominates in the kinetics of MO photocatalytic degradation. The intra-particle diffusion (corresponding to stage II on the kinetic curves) in the porous biosilica is insignificant.

2.2.3. MO Photocatalytic Degradation Depending on the MO Initial Concentration

The isotherm and efficiency of MO photocatalytic degradation under UV irradiation at 25 °C in the presence of PdCl₂ biosilica as a function of dye initial concentration are shown in Figures 7 and 8, respectively.

The isotherm of MO degradation in the presence of PdCl₂ biosilica photocatalyst was determined for the initial concentrations 5–200 mg/L. The results indicate that the amount of converted dye rises steeply with increasing dye initial concentration (Figure 7). Interestingly, the steep character of the slope of the isotherm of the photocatalytic degradation of MO remains even in the presence of the highest concentrations of the dye used in the experiment, which may indicate a sufficient energy potential of this photocatalyst for effective decomposition of even higher dye concentrations. The maximum conversion of MO

of 294 mg/g was reached in this experiment at 200 mg/L of the dye initial concentration. Three isotherm models (Langmuir, Freundlich, and Temkin) were applied to describe the experimental data. The results of the isotherm models fitting (Table 2) show that the MO degradation by PdCl₂ biosilica photocatalyst could be best described by the Temkin model with high determination coefficients. The fits to the Freundlich and Langmuir models were of poor quality, according to the evaluated fitting constants. According to the Temkin isotherm theory, we can assume similar values of energy of photocatalytic degradation process for the whole range of the used initial concentrations and the results indicate that this process is irreversible.

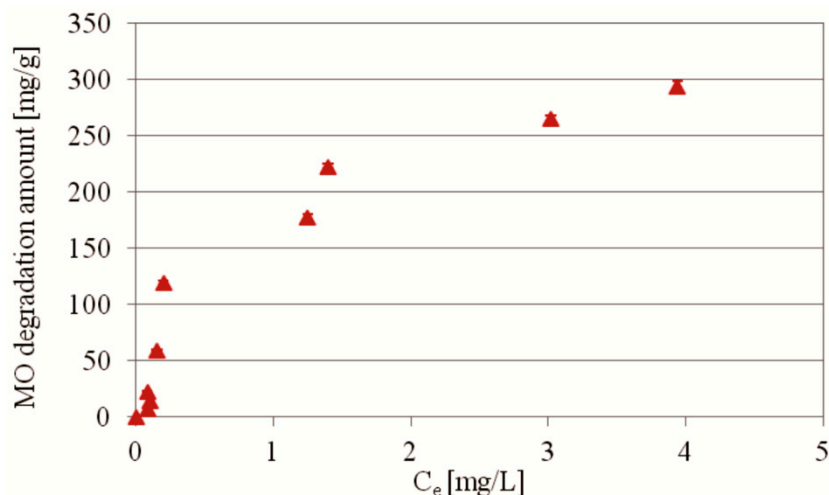


Figure 7. Isotherm of MO photocatalytic degradation as a function of the initial concentration of MO in the presence of PdCl₂ biosilica photocatalyst. Experimental conditions: m (biosilica)—10 mg; t = 75 min; T = 25 °C; C₀(MO)—5–200 mg/L; V (MO solution)—15 mL; pH—7.0.

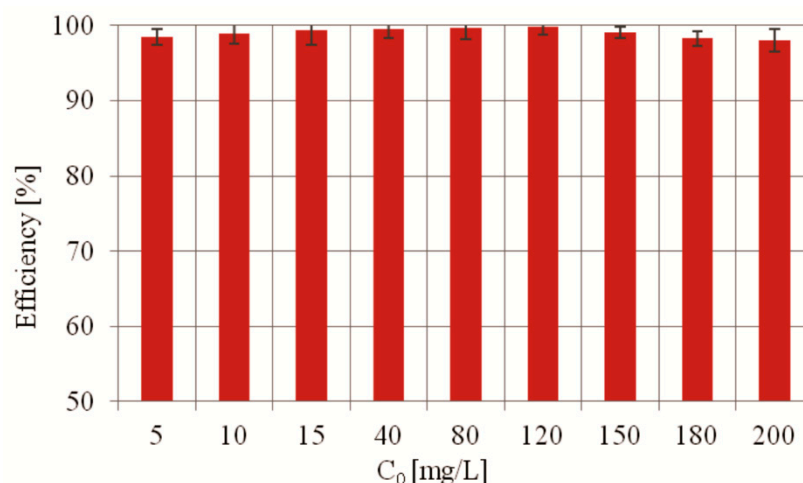


Figure 8. Efficiency of MO photocatalytic degradation as a function of the initial concentration of MO in the presence of PdCl₂ biosilica photocatalyst. Experimental conditions: m (biosilica)—10 mg; T = 25 °C; t = 75 min; C₀(MO)—5–200 mg/L; V (MO solution)—15 mL; pH—7.0.

The efficiency of MO degradation in the presence of PdCl₂ biosilica photocatalyst was determined to be at the level of 98–99.8% for the initial concentration ranges 5–200 mg/L (Figure 8). The results show that the degradation efficiency does not decrease appreciably with increasing MO initial concentration up to 200 mg/L. This phenomenon can be explained by the fact that the photocatalytic capacity of the synthesized catalyst is very high, and the dye degradation products do not interfere with the photocatalytic degradation process.

Table 2. The parameters of the MO photocatalytic degradation isotherm as determined from fitted isotherm models: C_e (mg/L) is the equilibrium concentration, q_m (mg/g) the maximum adsorption capacity, K_L (L/mg) the Langmuir constants, K_F (L/g) and $1/n$ are the Freundlich constants, BT is a constant related to the heat of adsorption and defined by the expression $BT = RT/b$, b is the Temkin constant (J/mol), A_T is the Temkin isotherm constant (L/g), T is the absolute temperature (K), and R is the gas constant (8.314 J/mol K).

Kinetics Model	Equation	Parameters	Value	R ²
PdCl2Biosilica25				
Langmuir	$C_e/q_e = (1/q_m K_L) + C_e/q_m$	K_L (L/mg) q_m (mg/g)	0.5442 434.8	0.5047
Freundlich	$\log q_e = \log K_F + 1/n \log C_e$	K_F (L/g) $1/n$	137.27 0.767	0.7707
Temkin	$q_e = B_T \ln A_T + B_T \ln C_e$	B_T (J/mol) A_T (L/g)	69.0 15.203	0.9634

According to the published reports, high effectiveness (80–99%) of MO photocatalytic degradation can be achieved also by employing other photocatalysts. The degradation efficiency 98% of MO photocatalytic degradation was reached using Fe_3O_4 nanoparticles [81], Pt modified TiO_2 [74], and TiO_2 -CuZSM-5 mixture [76], 99% by Ag/HSTiO₂ catalyst [70], and chitosan with immobilized nano-CdS photocatalyst [44], 96% by scoria-Ni/ TiO_2 [76], 93% by employing SiO_2 - TiO_2 photocatalyst [82], and 87% using Cu-doped ZnO nanoparticles [79]. Significantly lower efficiency (50–70%) of MO degradation was found when using such photocatalysts as Ag/ TiO_2 nanocomposites [83], anatase TiO_2 nanoparticles [80], $MnWO_4$ powder [68], and ZnO/GO and TiO_2 /ZnO/GO nanocomposite photocatalyst [84]. However, in order to improve the quality of most of the tested catalysts, it is necessary to reduce the photocatalytic degradation time and increase the recycling time.

2.2.4. The Recyclability of the Used PdCl₂ Biosilica Photocatalyst

The stability of photocatalyst recycling capacity is an important indicator of its possible application. Five cycling runs of the photocatalytic degradation of MO dye was performed to evaluate the photocatalytic stability of reused photocatalyst. The results concerning the reusability of PdCl₂ biosilica photocatalyst are shown in Figure 9. As indicated, a high MO photodegradation is maintained after five cycle rounds of the photocatalyst reuse, which proved that the prepared PdCl₂ biosilica photocatalyst has a very good recyclability. The fears that immobilized nanoparticles of palladium(II) chlorides may be insufficiently stable in an aqueous solution of the dye were not confirmed in our experiment.

Palladium(II) chloride anchored on polystyrene modified with 5-amino-1,10-phenanthroline (PS-phen/PdCl₂) was used as an efficient recoverable catalyst for Suzuki cross-coupling reactions and after the catalyst reuse in five cycles no significant Pd leaching and no loss of its catalytic activity were observed [43]. Moreover, a comparison of the catalytic performance of PS-phen/PdCl₂ and other supported Pd catalysts indicated that PS-phen/PdCl₂ was more active and more stable than the commonly used supported catalyst Pd/C [43]. This observation was explained by probable formation of covalent interactions between PdCl₂ and the nitrogen-containing ligand of the support [43]. A similar catalytic efficiency of Pd particles and PdCl₂ in the reduction of methylene blue by hydrazine has been reported by Aoki and co-authors [44].

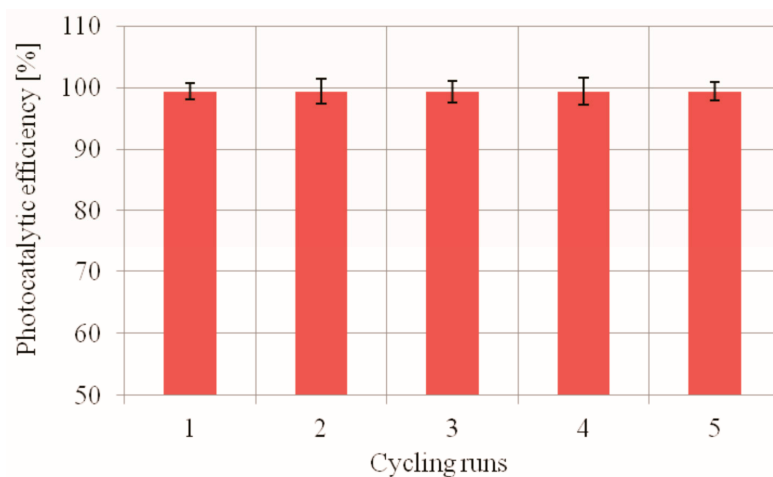


Figure 9. Efficiency of MO degradation as a function of UV irradiation time over PdCl₂ biosilica photocatalyst. Experimental conditions: m (biosilica)—10 mg; C₀(MO)—9.98 mg/L; T = 25 °C; t = 75 min; V (MO solution)—15 mL; pH—7.0.

2.3. Methyl Orange Degradation Products

Figure 10 presents the scheme of degradation of methyl orange (MO) obtained on the basis of the results of ESI-HRMS.

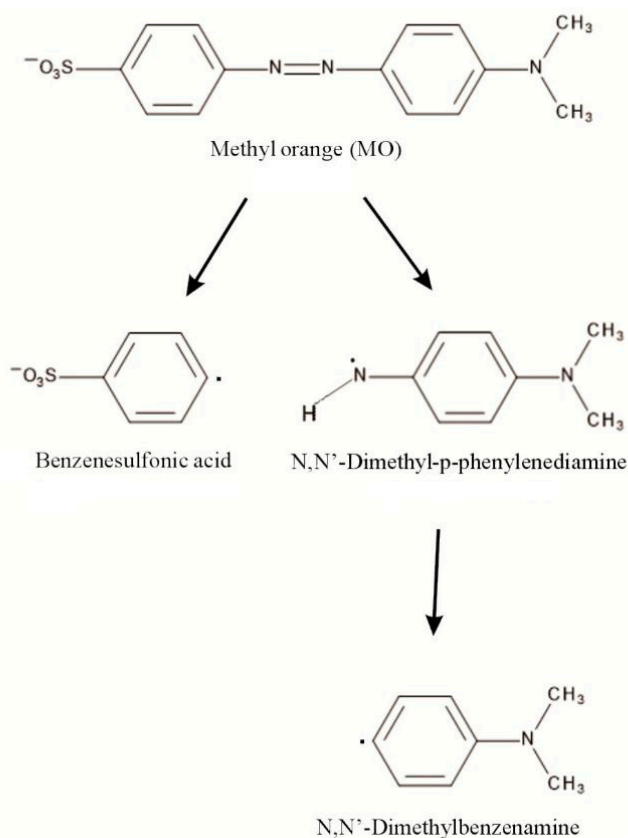


Figure 10. Degradation scheme of methyl orange (MO).

Electrospray Ionization–High-Resolution Mass Spectrometry (ESI-HRMS) for the standards of: methyl orange, benzenesulphonic acid, *N,N*-dimethyl-*p*-phenylenediamine and *N,N*-dimethylbenzenamine and MO reaction mixture was carried out in ESI(+), ESI(+)+FA (formic acid) and ESI(−) modes.

Methyl orange in ESI(−) mode gives a peak at a m/z value of 304.0760, with the molecular formula of $C_{14}H_{14}N_3SO_3$ (M_{MO} , Figure S1) and in ESI(+) or ESI(+) + FA it corresponds to m/z value of 306.0918 of the molecular formula of $C_{14}H_{16}N_3SO_3$ (M_{MOH_2} , Figures S6 and S11). A similar peak was detected at an m/z value of 304 for MO standard by Baiocchi et al. [85] using MS/MS and MS/MS/MS analyses in ESI(−) mode and at m/z ratio of 304.2 by Chen et al. [86] using MS/MS. The ion at m/z 156.9978 (M_{BA} , benzenesulphonic acid radical anion, ESI(−), Figure S2) corresponds to $[C_6H_5O_3S]$ and the ion at m/z 159.0107 (M_{BAH_2}) corresponds to $C_6H_5O_3SH_2$ (M_{BAH_2} , benzenesulphonic cation radical, ESI(+) or ESI(+) + FA, Figures S7 and S12). *N,N*-dimethyl-*p*-phenylenediamine protonated standard with m/z value of 137.1072 corresponding to $C_8H_{11}N_2H$ (M_{DH}), of the molecular formula of $C_8H_{13}N_2$ is detected in ESI(+) and ESI(+) + FA (Figure S8 and S13). The *N,N*-dimethyl-*p*-phenylenediamine radical anion standard of the molecular formula of $C_8H_{11}N_2H$ (M_D , $m/z = 135.0882$, ESI(−)) is shown in Figure S3.

The primary peak assigned to *N,N*-dimethylbenzenamine anion radical standard is detected in ESI(−) mode with m/z value of 120.0439 corresponding to $C_8H_{10}N$ (M_{DB} , Figure S4). In Figures S9 and S14, the ion at $m/z = 122.0969$ (ESI(+)) + (ESI(+) + FA), corresponding to *N,N*-dimethylbenzenamine radical cation standard of the molecular formula $C_8H_{10}NH_2$ (M_{DBH_2}), is shown.

The mass spectrum for the full-range scan of MO reaction in ESI(−) mode is shown in Figure S5. As the obtained results imply, the first stage of the methyl orange degradation involves the azo bond breaking, which leads to the formation of benzenesulphonic acid radical anion (m/z value of 156.9950). In negative-ion mode, only this peak is detected.

Similarly, in ESI(+) and ESI(+) + FA, a peak corresponding to benzenesulphonic acid radical cation is detected, as shown in Figures S10 and S15 ($m/z = 159.9701$). The peak at an m/z value of 122.0969 (M_{DBH_2}), shown in Figures S10 and S15, corresponds to the radical cation of *N,N*-dimethylbenzenamine. *N,N*-dimethyl-*p*-phenylenediamine radical cation with m/z value of 137.1072 (M_{DH_2}) corresponding to $C_8H_{13}N_2H$, with the molecular formula of $C_8H_{13}N_2$ is detected, as shown in Figures S10 and S15 [87]. Summary of ESI-HRMS results is presented in Table 3.

3. Materials and Methods

3.1. Preparation of the Photocatalyst

3.1.1. Diatom Biosilica

Diatom biosilica was obtained under laboratory conditions by cultivation of selected diatom species *Pseudostaurosira trainorii* (the Culture Collection of Baltic Algae, Institute of Oceanography, University of Gdańsk, Poland) according to the procedure described in the work of M. Sprynskyy and co-workers [39]. The diatom biosilica was fabricated in the form of single diatom frustules of elliptical shapes with an average valve length r 4–5 μ m. The diatom silica has a three-dimensional structure with silica walls perforated by spatially periodic network of oval pores with pore size range 150–200 nm [39,88]. According to X-ray diffraction analysis data, this biosilica was identified as hydrated silica like opal-A [39]. The physicochemical properties of the obtained biosilica are characterized in more detail in previously published works [39,88].

3.1.2. Palladium(II) Chloride-Doped Diatom Biosilica/Commercial Amorphous Silica

The synthesis of diatom biosilica doped with palladium(II) chloride was performed by dispersing the diatom biosilica or commercial amorphous silica (POCH) (0.5 g) using ultrasound bath for 3 h, in a mixture containing 75 mL of methanol (Honeywell) and palladium(II) chloride (1 wt.%; $PdCl_2$, Alfa Aesar, 99.9%). Next, the mixture was subjected to stirring for 24 h at 25 °C and then the catalysts were dried at 60 °C to evaporate the solvent.

Table 3. Summary of ESI-HRMS results.

<i>m/z</i>	Compound	ESI Mode	Molecular Formula	Symbolic Formula
304.0760	MO standard	(−)	C ₁₄ H ₁₄ N ₃ SO ₃	M _{MO}
306.0918	MO protonated standard fragmentation product	(+) and (+) + FA	C ₁₄ H ₁₆ N ₃ SO ₃	M _{MOH₂}
156.9966	Benzenesulphonic acid radical anion standard	(−)	C ₆ H ₅ O ₃ S	M _{BA}
159.0107	Benzenesulphonic acid protonated standard	(+) and (+) + FA	C ₆ H ₅ O ₃ SH ₂	M _{BAH₂}
135.0882	<i>N,N</i> -dimethyl- <i>p</i> -phenylenediamine radical anion standard	(−)	C ₈ H ₁₁ N ₂ H	M _D
137.1072	<i>N,N</i> -dimethyl- <i>p</i> -phenylenediamine radical cation standard	(+) and (+) + FA	C ₈ H ₁₁ N ₂ H ₂	M _{DH}
120.0439	<i>N,N</i> -dimethylbenzenamine anion radical standard	(−)	C ₈ H ₁₀ N	M _{DB}
122.0969	<i>N,N</i> -dimethylbenzenamine cation radical standard	(+) and (+) + FA	C ₈ H ₁₀ NH ₂	M _{DBH₂}

3.2. Photocatalyst Characterization

The crystal structure of the samples was investigated using X-ray diffraction (Bruker AXS D8 Advance diffractometer) with Cu K α (0.154 nm) radiation at a scan rate of $2\theta = 4\text{--}60^\circ$ with a step of 0.05° . The morphology and structure of the doped diatom biosilica, as well as palladium(II) chloride distribution in the synthesized catalysts, were examined by transmission electron microscopy (TEM, FEI Tecnai F20 X-Twin tool).

Low-temperature nitrogen adsorption/desorption isotherms were recorded on Quantachrome Autosorb iQ at -176°C , after prior degassing of the sample in vacuum at 120°C for 3 h. The surface area of the catalysts was determined by the BET (Brunauer–Emmett–Teller) method. The pore volume was determined using the KJS–BJH method based on the BJH (Barret–Joyner–Halenda) algorithm.

3.3. Photocatalytic Activity

The photocatalytic activity of palladium(II) chloride-doped biosilica (PdCl₂Biosilica), palladium(II) chloride and commercial amorphous silica doped with palladium(II) chloride (PdCl₂_SiO₂), was evaluated in photocatalytic degradation of methyl orange (Sigma-Aldrich, 4-[4-(Dimethylamino)phenylazo]benzenesulfonic acid sodium salt, MO) in water solution (pH7), hydrochloric acid solution (0.2 M; pH2, Stanlab) or sodium hydroxide solution (0.1 M; pH13, Stanlab) under UV light irradiation generated by a 125 W Hg lamp with a 365 nm cutoff filter.

In each experiment, 0.01 g of the photocatalyst was mixed with 15 mL of methyl orange solution (with various concentrations of MO: 5, 10, 15, 40, 80, 120, 150, 180, 200 mg L^{−1}). The process was conducted at three different temperatures: 25°C , 45°C and 65°C .

At irradiation time intervals of 0, 1, 5, 15, 35, 75, 135, 225, 345 and 525 min, the suspensions were collected and filtered to remove the photocatalyst particles. The MO concentrations were monitored at 464 nm during the adsorption/photodegradation process using a UV–Vis spectrophotometer (Varian Cary 50).

The Stability of the Used Photocatalysts

The PdCl₂ biosilica catalyst previously used in the process of MO degradation was subjected to regeneration. The process was carried out according to the description given in Section 2.3. Initially, the used catalyst was washed on a fine mesh size filter (to separate the catalyst from the MO solution). Next, the catalyst that remained on the filter was rinsed with ethanol and finally dried in a laboratory dryer. The regenerated catalyst was reused in the MO degradation process under identical conditions. The same catalyst was used 5 times, as this number of reuses was allowed by the amount of regenerated catalyst. The volume of MO solution used in the reaction was adjusted in proportion to the amount of the remaining catalyst.

3.4. Electrospray Ionization–High-Resolution Mass Spectrometry (ESI-HRMS)

To identify the photodegradation products of MO, Electrospray Ionization–High-Resolution Mass Spectrometry (ESI-HRMS) analyses were performed. After the photocatalysis process, the solution of MO was filtered through a 0.22 µm syringe filter (Chemland). The degradation products were identified according to the parameters described below. The measurements were carried out using a High-Resolution Triple TOF spectrometer (AB Sciex, 5600) in ESI negative, positive and positive with formic acid (HA) mode. Formic acid (1 µL/20 mL of sample) was added to facilitate ionization.

Each spectrum was scanned from 100 to 700 *m/z*.

4. Conclusions

The prepared diatom biosilica doped with palladium(II) chloride nanoparticles (PdCl₂Biosilica) is capable of acting as a highly efficient photocatalyst of MO degradation in water solution under UV light excitation. The palladium(II) chloride nanoparticles of irregular shapes with diameters ranging from 2 to 3 nm adhered tightly to the biosilica surface in the form of single-layer clusters.

The degradation efficiency was determined for PdCl₂ biosilica to be at a level of 98–99.8% for the MO initial concentration ranging from 5 to 200 mg/L with a maximum MO conversion of 294 mg/g. For comparison, the maximum MO degradation efficiency of 52% was detected for pure biosilica (biosilica). The degradation process was the most intense in a neutral medium at pH7. The recycling experiment showed the stability of the degradation efficiency for PdCl₂ biosilica after five consecutive runs.

The kinetics curves of MO photocatalytic degradation over PdCl₂ biosilica or biosilica can be divided into three different stages: initial rapid photocatalytic degradation, slowly running process, and the stage of equilibrium with weak fluctuation effects. The photocatalytic process was very fast and in the initial step the degradation efficiency reached about 45% for biosilica and 85% for PdCl₂ biosilica within the first minute.

PdCl₂ biosilica and biosilica showed negligible abilities to adsorb MO in the dark. The effect of UV radiation on the degradation of MO in the absence of a catalyst and the effect of temperature increase were also negligible. Therefore, it is reasonable to suppose that both HO• and O₂•[−] radicals, highly oxidizing species, can be generated on the biosilica surface by attacks of photons emitted from pure diatom biosilica under UV light excitation and involved in the photocatalytic processes of MO degradation (photonic scattering effect). The photocatalytic activity of PdCl₂ biosilica is effectively enhanced (over twice) compared to that of pure biosilica, which can be interpreted as a result of the photonic effect of palladium(II) chloride nanoparticles immobilized on biosilica (synergetic photonic scattering effect).

Supplementary Materials: The following are available online at <https://www.mdpi.com/article/10.3390/ijms22136734/s1>, Figure S1: ESI-MS(-) of MO standard with molecular formula C₁₄H₁₄N₃SO₃ (MMO, *m/z* = 304.0760), Figure S2: ESI-MS(-) of benzenesulphonic acid radical anion standard with molecular formula C₆H₅O₃S (MBA, *m/z* = 156.9978), Figure S3: ESI-MS(-) of N,N-dimethyl-p-phenylenediamine radical anion standard with molecular formula C₈H₁₁N₂H (MD, *m/z*=135.0882),

Figure S4: ESI-MS(-) of N,N-dimethylbenzenamine radical anion standard with molecular formula C₈H₁₀N (MDB, $m/z = 120.0439$), Figure S5: ESI-MS(-) of MO reaction mixture, Mass/Charge – 100-600 [Da], Figure S6: ESI-MS(+) of MO standard with molecular formula C₁₄H₁₆N₃SO₃ (MMOH₂, $m/z=306.0918$), Figure S7: ESI-MS(+) of benzenesulphonic acid radical cation standard with molecular formula C₆H₅O₃SH₂ (MBAH₂, $m/z = 159.0107$), Figure S8: ESI-MS(+) of N,N-dimethyl-p-phenylenediamine radical cation standard with molecular formula, C₈H₁₁N₂H₂ (MDH, $m/z = 137.1072$), Figure S9: ESI-MS(+) of N,N-dimethylbenzenamine radical cation standard with molecular formula C₈H₁₀NH₂ (MDBH₂, $m/z = 122.0969$), Figure S10: ESI-MS(+) of MO reaction mixture, Mass/Charge – 100-700 [Da], Figure S11: ESI-MS(+) + FA of MO standard with molecular formula C₁₄H₁₆N₃SO₃ (MMOH₂, $m/z=306.0918$), Figure S12: ESI-MS(+) + FA of benzenesulphonic acid radical cation standard with molecular formula C₆H₅O₃SH₂ (MBAH₂, $m/z = 159.0107$), Figure S13: ESI-MS(+) + FA of N,N-dimethyl-p-phenylenediamine radical cation standard with molecular formula, C₈H₁₁N₂H₂ (MDH, $m/z = 137.1072$), Figure S14: ESI-MS(+) + FA of N,N-dimethylbenzenamine radical cation standard with molecular formula C₈H₁₀NH₂ (MDBH₂, $m/z = 122.0969$), Figure S15: ESI-MS(+) + FA of MO reaction mixture, Mass/Charge – 100-700 [Da].

Author Contributions: M.S.: Conceptualization, Methodology, Investigation, Visualization, Data curation, Writing—original draft; P.S.: Methodology, Writing—editing; I.W.: Methodology; A.W.: Funding acquisition, Project administration, Writing—editing; B.B.: Funding acquisition, Project administration, Writing—editing; I.N.: Funding acquisition, Project administration, Writing—editing; A.F.-G.: Conceptualization, Methodology, Investigation, Visualization, Data curation, Writing—original draft. All authors have read and agreed to the published version of the manuscript.

Funding: The work was carried out within the project “Advanced biocomposites for tomorrow’s economy BIOG-NET” funded by Foundation for Polish Science from the European Regional Development Fund (POIR.04.04.00-00-1792/18-00).

Institutional Review Board Statement: Not applicable.

Informed Consent Statement: Not applicable.

Data Availability Statement: The data presented in this study are available upon request.

Conflicts of Interest: The authors declare no conflict of interest.

References

1. Robinson, T.; McMullan, G.; Marchant, R.; Nigam, P. Remediation of dyes in textile effluent: A critical review on current treatment technologies with a proposed alternative. *Bioresour. Technol.* **2001**, *77*, 247–255. [\[CrossRef\]](#)
2. Parshetti, G.K.; Telke, A.A.; Kalyani, D.C.; Govindwar, S.P. Decolorization and detoxification of sulfonated azo dye methyl orange by *Kocuria rosea* MTCC 1532. *J. Hazard. Mater.* **2010**, *176*, 503–509. [\[CrossRef\]](#)
3. Vitor, V.; Corso, C.R. Decolorization of textile dye by *Candida albicans* isolated from industrial effluents. *J. Ind. Microbiol. Biotechnol.* **2008**, *35*, 1353–1357. [\[CrossRef\]](#) [\[PubMed\]](#)
4. Saroj, S.; Kumar, K.; Pareek, V.; Prasad, R.; Singh, R.P. Biodegradation of azo dyes Acid Red 183, Direct Blue 15 and Direct Red 75 by the isolate *Penicillium oxalicum* SAR-3. *Chemosphere* **2014**, *107*, 240–248. [\[CrossRef\]](#) [\[PubMed\]](#)
5. Wu, Y.; Li, T.; Yang, L. Mechanisms of removing pollutants from aqueous solutions by microorganisms and their aggregates: A review. *Bioresour. Technol.* **2012**, *107*, 10–18. [\[CrossRef\]](#)
6. Boucherit, N.; Abouseoud, M.; Adour, L. Degradation of direct azo dye by *Cucurbita pepo* free and immobilized peroxidase. *J. Environ. Sci.* **2013**, *25*, 1235–1244. [\[CrossRef\]](#)
7. Konstantinou, I.K.; Albanis, T.A. TiO₂-assisted photocatalytic degradation of azo dyes in aqueous solution: Kinetic and mechanistic investigations: A review. *Appl. Catal. B Environ.* **2004**, *49*, 1–14. [\[CrossRef\]](#)
8. Daneshvar, N.; Salari, D.; Khataee, A.R. Photocatalytic degradation of azo dye acid red 14 in water: Investigation of the effect of operational parameters. *J. Photochem. Photobiol. A Chem.* **2003**, *157*, 111–116. [\[CrossRef\]](#)
9. Auta, M.; Hameed, B.H. Coalesced chitosan activated carbon composite for batch and fixed-bed adsorption of cationic and anionic dyes. *Colloids Surf. B Biointerfaces* **2013**, *105*, 199–206. [\[CrossRef\]](#) [\[PubMed\]](#)
10. Taghizadeh, F.; Ghaedi, M.; Kamali, K.; Sharifpour, E.; Sahraie, R.; Purkait, M.K. Comparison of nickel and/or zinc selenide nanoparticle loaded on activated carbon as efficient adsorbents for kinetic and equilibrium study of removal of Arsenazo (III) dye. *Powder Technol.* **2013**, *245*, 217–226. [\[CrossRef\]](#)
11. Koupaie, E.H.; Moghaddam, M.R.A.; Hashemi, S.H. Successful treatment of high azo dye concentration wastewater using combined anaerobic/aerobic granular activated carbon-sequencing batch biofilm reactor (GAC-SBBR): Simultaneous adsorption and biodegradation processes. *Water Sci. Technol.* **2013**, *67*, 1816–1821. [\[CrossRef\]](#)

12. Tabatabaee, M.; Ghotbifar, A.; Mozafari, A.A. Photocatalytic degradation and kinetic study of textile azo dyes direct blue 71 and black 19 in ZnO-suspended solution. *Fresenius Environ. Bull.* **2012**, *21*, 1468–1473.
13. Chatzisympson, E.; Petrou, C.; Mantzavinos, D. Photocatalytic treatment of textile dyehouse effluents with simulated and natural solar light. *Glob. Nest J.* **2013**, *15*, 21–28.
14. Pang, Y.L.; Abdullah, A.Z. Fe³⁺ doped TiO₂ nanotubes for combined adsorption-sonocatalytic degradation of real textile wastewater. *Appl. Catal. B Environ.* **2013**, *129*, 473–481. [[CrossRef](#)]
15. Carp, O.; Huisman, C.L.; Reller, A. Photoinduced reactivity of titanium dioxide. *Prog. Solid State Chem.* **2004**, *32*, 33–177. [[CrossRef](#)]
16. Shi, R.; Lin, J.; Wang, Y.J.; Xu, J.; Zhu, Y.F. Visible-Light Photocatalytic Degradation of BiTaO₄ Photocatalyst and Mechanism of Photocorrosion Suppression. *J. Phys. Chem. C* **2010**, *114*, 6472–6477. [[CrossRef](#)]
17. Ge, L.; Han, C.; Liu, J. Novel visible light-induced g-C₃N₄/Bi₂WO₆ composite photocatalysts for efficient degradation of methyl orange. *Appl. Catal. B Environ.* **2011**, *108–109*, 100–107. [[CrossRef](#)]
18. Hoffmann, M.R.; Martin, S.T.; Choi, W.; Bahnemann, D.W. Environmental Applications of Semiconductor Photocatalysis. *Chem. Rev.* **1995**, *95*, 69–96. [[CrossRef](#)]
19. Wang, P.; Huang, B.; Dai, Y.; Whangbo, M.-H. Plasmonic photocatalysts: Harvesting visible light with noble metal nanoparticles. *Phys. Chem. Chem. Phys.* **2012**, *14*, 9813–9825. [[CrossRef](#)]
20. Fan, W.; Leung, M.K.H. Recent Development of Plasmonic Resonance-Based Photocatalysis and Photovoltaics for Solar Utilization. *Molecules* **2016**, *21*, 180. [[CrossRef](#)]
21. Lv, K.; Perriman, A.W.; Mann, S. Photocatalytic multiphase micro-droplet reactors based on complex coacervation. *Chem. Commun.* **2015**, *51*, 8600–8602. [[CrossRef](#)]
22. Chen, L.; Tian, L.; Zhao, X.; Hu, Z.; Fan, J.; Lv, K. SPR effect of Au nanoparticles on the visible photocatalytic RhB degradation and NO oxidation over TiO₂ hollow nanoboxes. *Arab. J. Chem.* **2020**, *13*, 4404–4416. [[CrossRef](#)]
23. Ge, L.; Xu, M.X.; Fang, H.B. Synthesis of novel photocatalytic InVO₄-TiO₂ thin films with visible light photoactivity. *Mater. Lett.* **2007**, *61*, 63–66. [[CrossRef](#)]
24. Kudo, A.; Omori, K.; Kato, H. A Novel Aqueous Process for Preparation of Crystal Form-Controlled and Highly Crystalline BiVO₄ Powder from Layered Vanadates at Room Temperature and Its Photocatalytic and Photophysical Properties. *J. Am. Chem. Soc.* **1999**, *121*, 11459–11467. [[CrossRef](#)]
25. Lee, Y.L.; Chi, C.F.; Liao, S.Y. CdS/CdSe Co-Sensitized TiO₂ Photoelectrode for Efficient Hydrogen Generation in a Photoelectrochemical Cell. *Chem. Mater.* **2010**, *22*, 922–927. [[CrossRef](#)]
26. Ren, J.; Wang, W.Z.; Sun, S.M. Enhanced photocatalytic activity of Bi₂WO₆ loaded with Ag nanoparticles under visible light irradiation. *Appl. Catal. B Environ.* **2009**, *92*, 50–55. [[CrossRef](#)]
27. Wang, X.C.; Maeda, K.; Chen, X.F.; Takanebe, K.; Domen, K.; Hou, Y.D.; Fu, X.Z.; Antonietti, M. Polymer Semiconductors for Artificial Photosynthesis: Hydrogen Evolution by Mesoporous Graphitic Carbon Nitride with Visible Light. *J. Am. Chem. Soc.* **2009**, *131*, 1680–1681. [[CrossRef](#)] [[PubMed](#)]
28. Fang, S.; Lv, K.; Li, Q.; Ye, H.; Du, D.; Li, M. Effect of acid on the photocatalytic degradation of rhodamine B over g-C₃N₄. *Appl. Surf. Sci.* **2015**, *358*, 336–342. [[CrossRef](#)]
29. Fang, S.; Xia, Y.; Lv, K.; Li, Q.; Sun, J.; Li, M. Effect of carbon-dots modification on the structure and photocatalytic activity of g-C₃N₄. *Appl. Catal. B* **2016**, *185*, 225–232. [[CrossRef](#)]
30. Huo, Y.; Jin, Y.; Zhang, Y. Citric acid assisted solvothermal synthesis of BiFeO₃ microspheres with high visible-light photocatalytic activity. *J. Mol. Catal. A Chem.* **2010**, *331*, 15–20. [[CrossRef](#)]
31. Shan, A.Y.; Ghazi, T.I.M.; Rashid, S.A. Immobilisation of titanium dioxide onto supporting materials in heterogeneous photocatalysis: A review. *Appl. Catal. A Gen.* **2010**, *389*, 1–8. [[CrossRef](#)]
32. Round, F.E.; Crawford, R.M.; Mann, D.G. *Diatoms: Biology and Morphology of the Genera*; Cambridge University Press: Cambridge, UK, 1990.
33. Gordon, R.; Drum, R.W. The chemical basis of diatom morphogenesis. *Int. Rev. Cytol.* **1994**, *150*, 243–372.
34. Zhang, X.Y.; Suna, X.W. Diatom Nanotechnology: Progress and Emerging Applications. In *Nanoscience & Nanotechnology*, 4th ed.; Dusan, L., Ed.; The Royal Society of Chemistry: Cambridge, UK, 2018; pp. 175–200.
35. Ghobara, M.M.; Mazumder, N.; Vinayak, V.; Reissig, L.; Gebeshuber, I.C.; Tiffany, M.A.; Gordon, R. Diatoms: Fundamentals and Applications. In *On Light and Diatoms: A Photonics and Photobiology Review*; Joseph, S., Richard, G., Eds.; Wiley-Scrivener: Beverly, MA, USA, 2019; pp. 129–190.
36. Rorrer, G.L. Functionalization of Frustules from Diatom Cell Culture for Optoelectronic Properties. In *Nanoscience & Nanotechnology*, 4th ed.; Dusan, L., Ed.; The Royal Society of Chemistry: Cambridge, UK, 2018; pp. 79–110.
37. Gordon, R.; Losic, D.; Tiffany, M.A.; Nagy, S.S.; Sterrenburg, F.A.S. The Glass Menagerie: Diatoms for novel applications in nanotechnology. *Trends Biotechnol.* **2009**, *27*, 116–127. [[CrossRef](#)]
38. Umernura, K.; Gao, Y.; Nishikawa, T. Preparation of Photocatalyst Using Diatom Frustules by Liquid Phase Deposition Method. *J. Nanosci. Nanotechnol.* **2010**, *10*, 4883–4888. [[CrossRef](#)] [[PubMed](#)]
39. Sprynskyy, M.; Pomastowski, P.; Hornowska, M.; Król, A.; Rafińska, K.; Buszewski, B. Naturally organic functionalized 3D biosilica from diatom microalgae. *Mater. Des.* **2017**, *132*, 22–29. [[CrossRef](#)]
40. Schmid, G. Large clusters and colloids. Metals in the embryonic state. *Chem. Rev.* **1992**, *92*, 1709–1727. [[CrossRef](#)]

41. Bonnemann, H.; Brijoux, W.; Brinkmann, R.; Fretzen, R.; Jousen, T.; Koeppler, R.; Korall, B.; Neiteler, P. Richter Preparation, characterization, and application of fine metal particles and metal colloids using hydrotrioorganoborates. *J. Mol. Catal.* **1994**, *86*, 129–177. [[CrossRef](#)]
42. Li, F.; Zhang, B.; Dong, S.; Wang, E. A novel method of electrodepositing highly dispersed nano palladium particles on glassy carbon electrode. *Electrochim. Acta* **1997**, *42*, 2563–2568. [[CrossRef](#)]
43. Fan, G.; Zhang, H.; Cheng, S.; Ren, Z.; Hu, Z.; Wang, Z. Lewis Acid-Promoted Suzuki Reaction using Palladium Chloride Anchored on a Polymer as a Catalyst. *Aust. J. Chem.* **2008**, *61*, 610–614. [[CrossRef](#)]
44. Aoki, K.; Zhao, Y.; Chen, J. Colloidal submicron-palladium particles stabilized with acetate. *Electrochim. Acta* **2007**, *52*, 2485–2491. [[CrossRef](#)]
45. Van Eynde, E.; Tytgat, T.; Smits, M.; Verbruggen, S.W.; Hauchecorne, B.; Lenaerts, S. Biotemplated diatom silica-titania materials for air purification. *Photochem. Photobiol. Sci.* **2013**, *12*, 690–695. [[CrossRef](#)]
46. Ouwehand, J.; Van Eynde, E.; De Canck, E.; Lenaerts, S.; Verberckmoes, A.; Van Der Voort, P. Titania-functionalized diatom frustules as photocatalyst for indoor air purification. *Appl. Catal. B Environ.* **2018**, *226*, 303–310. [[CrossRef](#)]
47. He, J.; Chen, D.M.; Li, Y.L.; Shao, J.L.; Xie, J.; Sun, Y.J.; Yan, Z.Y.; Wang, J.Q. Diatom template TiO₂ with enhanced photocatalytic activity: Biomimetics of photonic crystals. *Appl. Phys. A* **2013**, *113*, 327–332. [[CrossRef](#)]
48. Padmanabhan, S.K.; Pal, S.; Haq, E.U.; Licciulli, A. Nanocrystalline TiO₂-diatomite composite catalysts: Effect of crystallization on the photocatalytic degradation of rhodamine B. *Appl. Catal. A* **2014**, *485*, 157–162. [[CrossRef](#)]
49. Mao, L.; Liu, J.; Zhu, S.; Zhang, D.; Chen, Z.; Chen, C. Sonochemical fabrication of mesoporous TiO₂ inside diatom frustules for photocatalyst. *Ultrason. Sonochem.* **2014**, *21*, 527–534. [[CrossRef](#)] [[PubMed](#)]
50. Van Eynde, E.; Hu, Z.-Y.; Tytgat, T.; Verbruggen, S.W.; Watté, J.; Van Tendeloo, G.; Van Driessche, I.; Blust, R.; Lenaerts, S. Diatom silica-titania photocatalysts for air purification by bio-accumulation of different titanium sources. *Environ. Sci. Nano* **2016**, *3*, 1052–1061. [[CrossRef](#)]
51. Kumari, S.; Min, K.H.; Kanth, B.K.; Jang, E.K.; Pack, S.P. Production of TiO₂-deposited Diatoms and Their Applications for Photo-catalytic Degradation of Aqueous Pollutants. *Biotechnol. Bioprocess Eng.* **2020**, *25*, 758–765. [[CrossRef](#)]
52. Gannavarapu, K.P.; Thakkar, M.; Veerapaga, S.; Wei, L.; Dandamudi, R.B.; Mitra, S. Novel diatom-FeOx composite as highly active catalyst in photodegradation of Rhodamine-6G. *Nanotechnol. Rev.* **2018**, *7*, 247–255. [[CrossRef](#)]
53. Uthappa, U.T.; Kigga, M.; Sriram, G.; Ajeya, K.V.; Jung, H.-Y.; Neelgund, G.M.; Kurkuri, M.D. Facile green synthetic approach of bio inspired polydopamine coated diatoms as a drug vehicle for controlled drug release and active catalyst for dye degradation. *Microporous Mesoporous Mater.* **2019**, *288*, 109572. [[CrossRef](#)]
54. Thommes, M.; Kaneko, K.; Neimark, A.V.; Olivier, J.P.; Rodriguez-Reinoso, F.; Rouquerol, J.; Sing, K.S.W. Physisorption of gases, with special reference to the evaluation of surface area and pore size distribution (IUPAC Technical Report). *Pure Appl. Chem.* **2015**, *87*, 1051–1069. [[CrossRef](#)]
55. Thommes, M. Physical Adsorption Characterization of Nanoporous Materials. *Chem. Ing. Tech.* **2010**, *82*, 1059–1073. [[CrossRef](#)]
56. Kruk, M.; Jaroniec, M.; Sayari, A. Application of large pore MCM-41 molecular sieves to improve pore size analysis using nitrogen adsorption measurements. *Langmuir* **1997**, *13*, 6267–6273. [[CrossRef](#)]
57. Al-Qaradawi, S.; Salman, S.R. Photocatalytic degradation of methyl orange as a model compound. *J. Photochem. Photobiol. A Chem.* **2002**, *148*, 161–168. [[CrossRef](#)]
58. Trabelsi, H.; Atheba, G.P.; Hentati, O.; Mariette, Y.D.; Robert, D.; Drogui, P.; Ksibi, M. Solar Photocatalytic Decolorization and Degradation of Methyl Orange Using Supported TiO₂. *J. Adv. Oxid. Technol.* **2016**, *19*, 79–84. [[CrossRef](#)]
59. Peng, H.H.; Chen, J.; Jiang, D.Y.; Li, M.; Feng, L.; Losic, D.; Dong, F.; Zhang, Y.X. Synergistic effect of manganese dioxide and diatomite for fast decolorization and high removal capacity of methyl orange. *J. Colloid Interface Sci.* **2016**, *484*, 1–9. [[CrossRef](#)]
60. Alabbad, E.A. Efficient Removal of Methyl Orange from Wastewater by Polymeric Chitosan-iso-vanillin. *Open Chem. J.* **2020**, *7*, 16–25. [[CrossRef](#)]
61. Tsuji, M.; Matsuda, K.; Tanaka, M.; Kuboyama, S.; Uto, K.; Wada, N.; Kawazumi, H.; Tsuji, T.; Ago, H.; Hayashi, J. Enhanced Photocatalytic Degradation of Methyl Orange by Au/TiO₂ Nanoparticles under Neutral and Acidic Solutions. *ChemistrySelect* **2018**, *3*, 1432–1438. [[CrossRef](#)]
62. Soto, A.I.; Valencia, R.N.A.; Vásquez, A.F.L. Effect of pH and Temperature on Photocatalytic Oxidation of Methyl Orange using Black Sand as Photocatalyst. *Rev. Mutis* **2018**, *8*, 43–54. [[CrossRef](#)]
63. Zhao, P.; Zhang, R.; Wang, J. Adsorption of methyl orange from aqueous solution using chitosan/diatomite composite. *Water Sci. Technol.* **2017**, *75*, 1633–1642. [[CrossRef](#)] [[PubMed](#)]
64. Szeto, W.; Kan, C.W.; Yuen, C.W.M.; Chan, S.-W.; Lam, K.H. Effective Photodegradation of Methyl Orange Using Fluidized Bed Reactor Loaded with Cross-Linked Chitosan Embedded Nano-CdS Photocatalyst. *Int. J. Chem. Eng.* **2014**, *2014*, 1–16. [[CrossRef](#)]
65. Xie, S.; Huang, P.; Kruzic, J.J.; Zeng, X.; Qian, H. A highly efficient degradation mechanism of methyl orange using Fe-based metallic glass powders. *Sci. Rep.* **2016**, *6*, 21947–21957. [[CrossRef](#)] [[PubMed](#)]
66. Rashed, M.N.; Eltahir, M.A.; Abdou, A.N.A. Adsorption and photocatalysis for methyl orange and Cd removal from wastewater using TiO₂/sewage sludge-based activated carbon nanocomposites. *R. Soc. Open Sci.* **2017**, *4*, 1–14. [[CrossRef](#)] [[PubMed](#)]
67. Mehra, M.; Sharma, T.R. Photo catalytic degradation of two commercial dyes in aqueous phase using photo catalyst TiO₂. *Adv. Appl. Sci. Res.* **2012**, *3*, 849–853.

68. He, H.Y.; Huang, J.F.; Cao, L.Y.; Wu, J.P. Photodegradation of methyl orange aqueous on MnWO_4 powder under different light resources and initial pH. *Desalination* **2010**, *252*, 66–70. [[CrossRef](#)]
69. Smith, Y.R.; Kar, A.; Subramanian, V.R. Investigation of Physicochemical Parameters That Influence Photocatalytic Degradation of Methyl Orange over TiO_2 Nanotubes. *Ind. Eng. Chem. Res.* **2009**, *48*, 10268–10276. [[CrossRef](#)]
70. Tokode, O.; Prabhu, R.; Lawton, L.A.; Robertson, P.K.J. The effect of pH on the photonic efficiency of the destruction of methyl orange under controlled periodic illumination with UV-LED sources. *Chem. Eng. J.* **2009**, *246*, 337–342. [[CrossRef](#)]
71. Sun, S.; Wang, W.; Zhang, L.; Xu, J. $\text{Bi}_2\text{WO}_6/\text{SiO}_2$ photonic crystal film with high photocatalytic activity under visible light irradiation. *Appl. Catal. B Environ.* **2012**, *125*, 144–148. [[CrossRef](#)]
72. Raja-Mogan, T.; Ohtani, B.; Kowalska, E. Photonic Crystals for Plasmonic Photocatalysis. *Catalysts* **2020**, *10*, 827. [[CrossRef](#)]
73. Huang, M.; Xu, C.; Wu, Z.; Huang, Y.; Lin, J.; Wu, J. Photocatalytic discolorization of methyl orange solution by Pt modified TiO_2 loaded on natural zeolite. *Dye. Pigment.* **2008**, *77*, 327–334. [[CrossRef](#)]
74. Li, M.; Guan, R.; Li, J.; Zhao, Z.; Zhang, J.; Qi, Y.; Zhai, H.; Wan, L. Photocatalytic Performance and Mechanism Research of Ag/HSTiO₂ on Degradation of Methyl Orange. *ACS Omega* **2020**, *5*, 21451–21457. [[CrossRef](#)]
75. Yang, L.; Chen, J.; Zhang, W. Adsorption and Photocatalytic Degradation of Methyl Orange on TiO_2 and CuZSM-5 Mixture. *Appl. Mech. Mater.* **2011**, *48–49*, 149–152. [[CrossRef](#)]
76. Pirsaeheb, M.; Hossaini, H.; Nasser, S.; Azizi, N.; Shahmoradi, B.; Khosravi, T. Optimization of photocatalytic degradation of methyl orange using immobilized scoria-Ni/ TiO_2 nanoparticles. *J. Nanostruct. Chem.* **2020**, *10*, 143–159. [[CrossRef](#)]
77. Zha, R.; Nadimicherla, R.; Guo, X. Ultraviolet photocatalytic degradation of methyl orange by nanostructured TiO_2/ZnO heterojunctions. *J. Mater. Chem. A* **2015**, *3*, 6565–6574. [[CrossRef](#)]
78. Lin, C.; Gao, Y.; Zhang, J.; Xue, D.; Fang, H.; Tian, J.; Zhou, C.; Zhang, C.; Li, Y.; Li, H. GO/ TiO_2 composites as a highly active photocatalyst for the degradation of methyl orange. *J. Mater. Res.* **2020**, *35*, 1307–1315. [[CrossRef](#)]
79. Fu, M.; Li, Y.; Wu, S.; Lu, P.; Liu, J.; Dong, F. Sol-gel preparation and enhanced photocatalytic performance of Cu-doped ZnO nanoparticles. *Appl. Surf. Sci.* **2011**, *258*, 1587–1591. [[CrossRef](#)]
80. Dhanalakshmi, J.; Padiyan, D.P. Photocatalytic degradation of methyl orange and bromophenol blue dyes in water using sol-gel synthesized TiO_2 nanoparticles. *Mater. Res. Express* **2017**, *4*, 1–9. [[CrossRef](#)]
81. Al-Abdallat, Y.; Jum'ah, I.; Bsoul, A.A.; Jumah, R.; Telfah, A. Photocatalytic Degradation Dynamics of Methyl Orange Using Coprecipitation Synthesized Fe_3O_4 Nanoparticles. *Water Air Soil Pollut.* **2019**, *230*, 277–293. [[CrossRef](#)]
82. Zhou, L.; Han, X.; Zhang, W.; He, H. Characterization of $\text{SiO}_2\text{-TiO}_2$ and photocatalytic degradation of methyl orange. *Asian J. Chem.* **2013**, *26*, 3837–3839. [[CrossRef](#)]
83. Zheng, X.; Zhang, D.; Gao, Y.; Wu, Y.; Liu, Q.; Zhu, X. Synthesis and characterization of cubic Ag/ TiO_2 nanocomposites for the photocatalytic degradation of methyl orange in aqueous solutions. *Inorg. Chem. Commun.* **2019**, *110*, 107589–107596. [[CrossRef](#)]
84. Raliya, R.; Avery, C.; Chakrabarti, S.; Biswas, P. Photocatalytic degradation of methyl orange dye by pristine titanium dioxide, zinc oxide, and graphene oxide nanostructures and their composites under visible light irradiation. *Appl. Nanosci.* **2017**, *7*, 253–259. [[CrossRef](#)]
85. Baiocchi, C.; Brussino, M.C.; Pramauro, E.; Prevot, A.B.; Palmisano, L.; Marci, G. Characterization of methyl orange and its photocatalytic degradation products by HPLC/UV-VIS diode array and atmospheric pressure ionization quadrupole ion trap mass spectrometry. *Int. J. Mass Spectrom.* **2002**, *214*, 247–256. [[CrossRef](#)]
86. Chen, T.; Zheng, Y.; Lin, J.M.; Chen, G. Study on the photocatalytic degradation of methyl orange in water using Ag/ZnO as catalyst by liquid chromatography electrospray ionization ion-trap mass spectrometry. *J. Am. Soc. Mass Spectrom.* **2008**, *19*, 997–1003. [[CrossRef](#)]
87. Shen, T.; Jiang, C.; Wang, C.; Sun, J.; Wang, X.; Li, X. A TiO_2 modified abiotic-biotic process for the degradation of the azo dye methyl orange. *RSC Adv.* **2015**, *5*, 58704–58712. [[CrossRef](#)]
88. Nowak, A.P.; Sprynskyy, M.; Brzozowska, W.; Lisowska-Oleksiak, A. Electrochemical behavior of a composite material containing 3D-structured diatom biosilica. *Algal Res.* **2019**, *41*, 101538–101544. [[CrossRef](#)]